

## Journal Pre-proofs

Stabilizing Anionic Redox Processes in Electrospun NiS<sub>2</sub> –based Cathode towards Durable Aluminum-ion Batteries

Junfeng Li, Kwan San Hui, Yunshan Zheng, Shunping Ji, Kaixi Wang, Chenyang Zha, Duc Anh Dinh, Xi Fan, Fuming Chen, Zongping Shao, Kwun Nam Hui

PII: S1385-8947(22)03720-2  
DOI: <https://doi.org/10.1016/j.cej.2022.138237>  
Reference: CEJ 138237

To appear in: *Chemical Engineering Journal*

Received Date: 20 April 2022  
Revised Date: 25 June 2022  
Accepted Date: 19 July 2022

Please cite this article as: J. Li, K. San Hui, Y. Zheng, S. Ji, K. Wang, C. Zha, D. Anh Dinh, X. Fan, F. Chen, Z. Shao, K. Nam Hui, Stabilizing Anionic Redox Processes in Electrospun NiS<sub>2</sub> –based Cathode towards Durable Aluminum-ion Batteries, *Chemical Engineering Journal* (2022), doi: <https://doi.org/10.1016/j.cej.2022.138237>

This is a PDF file of an article that has undergone enhancements after acceptance, such as the addition of a cover page and metadata, and formatting for readability, but it is not yet the definitive version of record. This version will undergo additional copyediting, typesetting and review before it is published in its final form, but we are providing this version to give early visibility of the article. Please note that, during the production process, errors may be discovered which could affect the content, and all legal disclaimers that apply to the journal pertain.

© 2022 Published by Elsevier B.V.



**Stabilizing Anionic Redox Processes in Electrospun NiS<sub>2</sub>-based Cathode towards  
Durable Aluminum-ion Batteries**

Junfeng Li<sup>a</sup>, Kwan San Hui<sup>b,\*</sup>, Yunshan Zheng<sup>a</sup>, Shunping Ji<sup>a</sup>, Kaixi Wang<sup>a</sup>, Chenyang  
Zha<sup>a</sup>, Duc Anh Dinh<sup>c</sup>, Xi Fan<sup>d</sup>, Fuming Chen<sup>e</sup>, Zongping Shao<sup>f,\*</sup> and Kwun Nam Hui<sup>a,\*</sup>

<sup>a</sup> Joint Key Laboratory of the Ministry of Education, Institute of Applied Physics and  
Materials Engineering, University of Macau, Avenida da Universidade, Taipa, Macau  
SAR, P.R. China

<sup>b</sup> School of Engineering, Faculty of Science, University of East Anglia, Norwich, NR4  
7TJ, United Kingdom

<sup>c</sup> NTT Hi-Tech Institute, Nguyen Tat Thanh University, Ho Chi Minh city 700000,  
Vietnam

<sup>d</sup> Ningbo Institute of Materials Technology, Engineering, Chinese Academy of  
Sciences, Ningbo, 315201, P.R. China

<sup>e</sup> Guangdong Provincial Key Laboratory of Quantum Engineering and Quantum  
Materials, School of Physics and Telecommunication Engineering, South China  
Normal University, P.R. China, 510006.

<sup>f</sup> WA School of Mines: Minerals, Energy and Chemical Engineering (WASM-MECE),  
Curtin University, Perth, WA 6845, Australia

**Abstract**

Rechargeable aluminum-ion batteries (AIBs) are receiving considerable attention as a desirable device for large-scale energy storage owing to high theoretical capacity and abundance of aluminum. However, due to strong charge of  $\text{Al}^{3+}$ , the state-of-the-art AIBs often show sluggish electrode reaction kinetics and rapid capacity fading and the available cathode materials always demonstrate poor structural stability, thereby greatly hindering their practical use.  $\text{NiS}_2$  with anion redox species ( $\text{S}_2^{2-}$  dimers) and favorable electronic conductivity is a promising cathode to boost the performance of AIBs in terms of reversible capacity, rate capability and cycling stability. Here, we report a systematic investigation of the Al storage behavior and mechanism of  $\text{NiS}_2/\text{S}$ -doped carbon ( $\text{NiS}_2/\text{SC}$ ) cathode based on a series of electrochemical tests and *ex situ* measurements. We further develop electrospun  $\text{NiS}_2/\text{S}$ -doped carbon@S-doped carbon nanofiber ( $\text{NiS}_2/\text{SC}@\text{SCNF}$ ) structure as the cathode of AIBs. The as-fabricated AIB delivers an unprecedented  $\text{Al}^{3+}$  storage performance with a stable capacity of 76 mAh  $\text{g}^{-1}$  at 0.5 A  $\text{g}^{-1}$  CV 500 cycles and a superior cycling Coulombic efficiency of 97%. This study reveals that  $\text{NiS}_2/\text{SC}@\text{SCNF}$  undergoes a reversible evolution of initial  $\text{Al}^{3+}$  insertion followed by anionic redox between  $\text{S}_2^{2-}$  and  $\text{S}^{2-}$ , paving the road for the further development of  $\text{NiS}_2$ -based cathodes for AIBs.

**Key words:** anionic redox, aluminum-ion batteries,  $\text{NiS}_2$ -based electrode, electrospun

## 1. Introduction

Because of their high intrinsic safety, high energy density, and lower costs, aluminum-ion batteries (AIBs) have received new attention during the past decade.[1-3] Aluminum is the most abundant metal on earth. Because Al can be triple-charged, it offers a high theoretical volumetric capacity of  $8046 \text{ mAh cm}^{-3}$  as an anode in the battery. In addition, its lower reactivity than lithium makes AIBs higher intrinsic safety than lithium-ion batteries. However, the practical use of AIBs is greatly hindered by the lack of high-performance cathode materials. The available cathodes usually show low capacity and poor reversibility during the electrochemical process, owing to the high electronegativity of the triple-charged  $\text{Al}^{3+}$  which causes the strong interaction of  $\text{Al}^{3+}$  with the structure of cathode material.[4-6] As compared to oxides, transition-metal sulfides (TMSs) have a softer anionic structure, thus energy barrier of  $\text{Al}^{3+}$  diffusion in TMSs is lower than in oxides, resulting in higher capacity and durability.[7-10] During the past, considerable efforts have been devoted to investigating the Al-ion storage mechanisms in metal sulfide-based electrodes. Both conversion-type and intercalation-type metal sulfides were observed, such as NiS[11],  $\text{Ni}_2\text{S}_3$ /graphene[12], and CuS[13] for the former, and  $\text{SnS}_2$ [14] and  $\text{WS}_2$ [15] for the latter ( $\text{AlCl}_4^-$ ). The aim is to accomplish high energy density or prevent the strong electrostatic interaction between Al-based ions and the host material.

Recently, the combination of cationic–anionic redox transformation or the exclusive anionic redox processes has been exhibited in multivalent metal-ion (such as

$\text{Ca}^{2+}$ ,  $\text{Mg}^{2+}$ , and  $\text{Al}^{3+}$ ) batteries to achieve high specific capacity.[16] In some metal sulfides (e.g.,  $\text{FeS}_2$ ,  $\text{Fe}_{0.5}\text{Co}_{0.5}\text{S}_2$ ,  $\text{TiS}_4$ , and  $\text{VS}_4$ )[17-22],  $\text{S}_2^{2-}$  dimers act as the main redox centers to promote the anionic redox processes, resulting in accelerated multielectron-transfer efficiency and enhanced storage capacity. In AIBs, the high-capacity  $\text{FeS}_2$  cathode has been investigated by X-ray absorption near-edge structure analysis. Reduced sulfur in the vicinity of the surface to form amorphous  $\text{Al}_2\text{S}_3$  and low crystalline  $\text{FeS}$  was observed.[17] Moreover, amorphous  $\text{TiS}_4$  cathode with anion enrichment achieved a high capacity of  $206 \text{ mAh g}^{-1}$  over 1000 cycles.[18] It was found that, during the storage of Al ions, the  $\text{TiS}_4$  cathode underwent a reversible anionic redox between  $\text{S}_2^{2-}$  and  $\text{S}^{2-}$ , which was accompanied by the dissociation of S-S bonds to form Al-S bonds and a decrease in Ti coordination number.

Among the various sulfides,  $\text{NiS}_2$ , belonging to the nickel sulfide family ( $\text{NiS}$ ,  $\text{NiS}_2$ ,  $\text{Ni}_3\text{S}_2$ , and  $\text{Ni}_3\text{S}_4$ ), has great potential as anode material in alkali-metal batteries because of its high theoretical capacity and abundance in resource.[23-25] Notably, owing to the high sulfur ratio in  $\text{NiS}_2$ , the energy overlapping between the Ni d levels and the sulfur valence band could facilitate the formation of  $\text{S}_2^{2-}$  dimers. [19, 26, 27] However, the anionic redox mechanism of the  $\text{NiS}_2$ -based materials in AIBs has not been fully explored.

In the present study, we reported in detail, for the first time, the storage mechanism of  $\text{NiS}_2$ -based cathode materials for AIBs. The redox processes and structural

transformations were systematically investigated through a series of *ex situ* measurements after the intercalation/deintercalation of Al ions in NiS<sub>2</sub>/S-doped carbon (NiS<sub>2</sub>/SC) material. The capacity-deterioration mechanisms of the NiS<sub>2</sub>/SC material were also elucidated. During discharge, the Al ions destroyed the NiS<sub>2</sub> crystal structure and were trapped in the subsequent charging process; at high charge voltage, Al-ion extraction caused the formation of active polysulfide species. This species subsequently dissolved into the electrolyte, resulting in the loss of active material. Notably, the merit of the thin layer of S-doped carbon (SC) coated onto NiS<sub>2</sub> helped to avoid the agglomeration of active materials and increase the interfacial area between the NiS<sub>2</sub> material and the electrolyte. To effectively utilize the active mass of the NiS<sub>2</sub> electrode and enhance the conductivity of the cathode electrode, electrospinning approach was then used to fabricate the NiS<sub>2</sub>/SC@SC nanofiber (NiS<sub>2</sub>/SC@SCNF) electrode. This electrode facilitated the rapid electron transfers and mass transports, as well as stabilized the anionic redox process by wrapping the soluble polysulfides species. As a new class cathode material for AIBs, an improved discharge capacity of 76 mAh g<sup>-1</sup> was achieved after 500 cycles at 500 mA g<sup>-1</sup> with a superior cycling Coulombic efficiency of 97%.

## 2. Experimental section

### 2.1. Preparation of Ni-TA coordination compounds

In a conventional method, 4.00 g of tannic acid (TA, AR) and 3.6 g of nickel nitrate hexahydrate (Ni(NO<sub>3</sub>)<sub>2</sub>•6H<sub>2</sub>O, 99%) were firstly dissolved in 60 mL of deionized (DI)

water to form solution A. In addition, 1.34 g of sodium hydroxide was dissolved in 20 mL of DI water to form solution B. Then solution A was added into solution B under magnetic stirring and vigorous stir was continued for 1 hour. Subsequently, the product was collected by high-speed centrifuge and washed with DI water and anhydrous alcohol several times. The metal-organic coordination compounds were finally obtained by freeze-drying.

## 2.2. Preparation of $\text{NiS}_2/\text{SC}$ and $\text{NiS}_2$

Firstly, the obtained Ni-TA coordination compounds were carbonized to form a Ni-catalyzed graphite layer along with the inside growth of Ni nanoparticles under nitrogen protection at 400 °C for 2 hours with a ramp rate of 2 °C min<sup>-1</sup> and then 800 °C for 2 hours with a ramp rate of 5 °C min<sup>-1</sup>, which were named Ni/C. The resulting Ni/C black powder and sublimed sulfur ( $\text{S}_8$ , 99.95%) were mixed with a mass ratio of 1:15 and entirely ground in mortar for 30 mins. Afterward, the mixture was heated at 350 °C for 2 h in a nitrogen atmosphere with a ramp rate of 2 °C min<sup>-1</sup> to obtain  $\text{NiS}_2/\text{SC}$ . For the preparation of  $\text{NiS}_2$ , the Ni/C powder was oxidized at 350 °C for 2h in an air atmosphere to remove the outer carbon and transform them into the NiO materials, and then the NiO powder was executed the same sulfuration procedure as the synthesis of  $\text{NiS}_2/\text{SC}$  to obtain pure  $\text{NiS}_2$ .

## 2.3. Preparation of $\text{NiS}_2/\text{SC}@/\text{SCNF}$

0.5 g PAN (polyacrylonitrile, Mw 150000) was firstly dissolved in DMF (N,N-

dimethylformamide, 4.5 mL) to obtain an 11 wt% PAN solution, and 0.25g of Ni/C was then added into the PAN solution with continuously magnetic stirring for 6 h. The resulting solution was loaded into a 5mL syringe for electrospinning with a 21-gauge stainless steel needle. Between the needle and the collector, the voltage of +19kV and -2kV was applied and the 15 cm distance was maintained. The electrospinning process was executed with a feeding rate of 20  $\mu\text{L}/\text{min}$ , a humidity of  $30 \pm 2.5 \%$  and a temperature of  $35 \pm 2 \text{ }^\circ\text{C}$ . After electrospinning, the obtained fibers were stabilized under nitrogen protection at  $280 \text{ }^\circ\text{C}$  for 2h with a ramp rate of  $2 \text{ }^\circ\text{C min}^{-1}$  and then pyrolyzed at  $800 \text{ }^\circ\text{C}$  for 1h with a ramp rate of  $5 \text{ }^\circ\text{C min}^{-1}$  to obtain Ni/C@CNF (carbon nanofiber). The same sulfidation process was carried out at  $350 \text{ }^\circ\text{C}$  for 2h in  $\text{N}_2$  atmosphere with the mixture of Ni/C@CNF and sulfur to obtain  $\text{NiS}_2/\text{SC@SCNF}$ .

#### 2.4. Fabrication of ionic liquid electrolyte

In an argon atmosphere glove box ( $[\text{O}_2] < 0.1 \text{ ppm}$ ,  $[\text{H}_2\text{O}] < 0.1 \text{ ppm}$ ), the  $[\text{EMIm}]\text{Al}_x\text{Cl}_y$  ionic liquid electrolyte was fabricated by sluggishly adding aluminum chloride ( $\text{AlCl}_3$ , 99%) into 1-Ethyl-3-methylimidazolium Chloride ( $[\text{EMIm}]\text{Cl}$ , 98.0%) with a molar ratio of 1.3. The addition process must be carried out slowly with constant stirring to avoid a vigorous exothermal reaction, then the light-yellow and transparent ionic liquids were obtained. Afterward, the obtained ionic liquid electrolyte was purified with one high-purity Al pellet (Al, 99.999%) at  $60^\circ\text{C}$  for 24h until it was nearly colorless.

### 2.5. Assembly of Aluminum-Ion Batteries

In a typical procedure, all the cathode was prepared by mixing a slurry of 70% active materials, 20% super P, and 10% PVDF in NMP solvent. After that, the slurry was coated on Mo current collector and dried at 80 °C for 12h in a vacuum. The loading mass in batteries is 0.78-1.06 mg cm<sup>-2</sup>. The soft-package batteries were assembled using the as-prepared electrodes as the cathodes, the metallic Al as the anode, and the glass fiber (GF/D) as the separator, then were injected with ~500 μL electrolyte in the glovebox.

### 2.6. Electrochemical measurements

For the galvanostatic discharge/charge tests, they were all conducted employing a Neware battery test system (BTS-53, Shenzhen, China) with the soft-package cells. It is worth noting that all galvanostatic long-cycling measurements were executed after a five-cycle activation process at current density of 0.2 A g<sup>-1</sup>. And the rate performance measurements were executed after a five-cycle activation process at a small current density of 0.1 A g<sup>-1</sup>. The cyclic voltammetry (CV) test was investigated in the range of 0-2.0 V at different scan rates. And under the open circuit potential, electrochemical impedance spectroscopy (EIS) spectra were collected with a frequency range of 10<sup>5</sup> to 0.1 Hz. All electrochemical measurements were performed using a BioLogic VMP-300 electrochemical workstation.

### 2.7. Characterization Techniques

The phase structure was determined by X-ray diffraction (Rigaku SmartLab, XRD) with Cu K $\alpha$  radiation from 10° to 90°. The morphologies and microstructures of materials were characterized by field emission scanning electron microscopy (Zeiss Sigma, FESEM) and transmission electron microscopy (JEM-F200, TEM) coupled with EDX spectroscopy. The micro Raman system (Horiba, LABHRev-UV) was used to acquire Raman spectra (200-700 cm<sup>-1</sup>). X-ray photoelectron spectroscopy (XPS) was conducted with a Thermo Fisher Scientific using an Al K $\alpha$  source, and binding energies were calibrated using carbon (C 1s=284.8 eV). All XPS samples after the electrochemical process were prepared in a glove box and transferred into a special chamber under an argon atmosphere without exposure to the air to reduce contamination and their XPS patterns were collected after a 60s etch time (Ion energy: 2000 eV; Sputter rate estimate: Ta<sub>2</sub>O<sub>5</sub> = 0.19 nm/s) to explain the anionic redox process. Thermogravimetric analysis (TGA) was conducted on an SDT-Q600 thermal analyzer with a heating speed of 10 °C min<sup>-1</sup> in airflow of 100 ml min<sup>-1</sup>. The NiS<sub>2</sub> mass percent can be described NiS<sub>2</sub> (wt.%) =  $\frac{\text{molecular of NiS}_2}{\text{molecular of NiO}}$  x residual weight (wt.%). To characterize the electrode after cycling, the cell was charged or discharged to different states at a current density of 200 mA g<sup>-1</sup> after a five-cycle activation process. Then the tested electrodes were disassembled, rinsed in anhydrous alcohol, and dried in the glovebox.

### 3. Results and discussion

To reveal the electrochemical reaction mechanism of NiS<sub>2</sub>-based materials as

cathode of AIBs, NiS<sub>2</sub>/SC material was synthesized by a conventional method in which Ni-TA coordination compounds were carbonized to obtain the Ni-catalyzed graphitic carbon embracing the Ni nanoparticles. Subsequently, the metallic Ni was transformed into NiS<sub>2</sub> through a simple sulfidation process (Fig. 1a). Fig. 1b shows the X-ray diffraction (XRD) pattern of the as-prepared NiS<sub>2</sub>/SC nanomaterial, which can be indexed based on the physical mixture of vaesite-type NiS<sub>2</sub> phase (PDF Card No. 11-0099) and graphite. The refined results revealed that the crystal structure of the NiS<sub>2</sub> phase in the composite is a cubic (*Pa-3*) unit cell with a lattice parameter of 5.68 Å. After the sulfidation at 350 °C and 15:1 (S<sub>8</sub>:Ni/C) mass ratio, pure-phase and high-crystallinity NiS<sub>2</sub>/SC was obtained (Fig. S1). With the further increase in ratio of sulfur to active material (a mass ratio of 20:1 (S<sub>8</sub>:Ni/C)) and sulfidation time, the typical characteristic peaks of NiS<sub>2</sub>/SC material remained the same, indicating the difficulty in forming higher S-rich nickel polysulfides (ratio > 2). According to the scanning electron microscopy (SEM) images as shown in Fig. 1c, a homogeneous and polygon-like morphology of the as-synthesized NiS<sub>2</sub>/SC material with a diameter of 50–300 nm was observed. Conversely, NiS<sub>2</sub> without SC could be obtained through the oxidization of Ni/C and the subsequent sulfidation of NiO (Figs. S2a and S2b). However, the NiS<sub>2</sub> material without the SC layer had a larger particle size and inhomogeneous particulate morphology with severe agglomeration (Fig. S2c). High-resolution transmission electron microscopy (HRTEM) showed that the SC had a NiS<sub>2</sub> core comprising a ~10 nm layer on the boundary (Figs. 1d and 1e). Furthermore, we observed clear lattice fringes with an interplanar spacing of 0.204 nm corresponding with the typical (220)

lattice plane of NiS<sub>2</sub>, and the long-range order stacking parallel carbon layer with an average interplanar spacing of 0.37 nm is in well agreement with a previously reported graphite material.[28, 29] Fig. 1f shows that the nickel and sulfur elements of the NiS<sub>2</sub>/SC material were coexistent and homogeneously distributed in the core. Similarly, HRTEM and EDS showed that the NiS<sub>2</sub> materials had a typical (200) lattice plane without a carbon layer (Figs. S2d, S2e, and S2f). The coating of the SC layer on NiS<sub>2</sub> could effectively reduce the particle size of NiS<sub>2</sub> and increase the interfacial area between the NiS<sub>2</sub> material and the electrolyte, which was very beneficial to electrochemical performance.[25]

Thermogravimetric analysis (TGA) was performed to examine carbon content of NiS<sub>2</sub>/SC material. Fig. 2a shows the TGA curve after the calcination from room temperature to 900 °C with flowing air. The final composition of NiO after the TGA test was determined through XRD analysis (Fig. S3). The weight loss can be correlated with the loss of adsorbed water, the combustion of the SC, and the conversion of NiS<sub>2</sub> into NiO. From the TGA curve, the weight loss of NiS<sub>2</sub>/SC is 62.4%. By calculating the mole ratio of active materials, the active mass percentage of NiS<sub>2</sub>/SC is 61.8%, and the corresponding mass percentage of carbon is 38.2%. The graphitic structure of the carbon layer was also verified by Raman spectroscopy; the peak at around 2700 cm<sup>-1</sup> corresponded with a typical 2D peak of the graphitic structure (Fig. 2b). The pattern showed two other obvious peaks at 1342 and 1569 cm<sup>-1</sup>, which were ascribed to the D and G bands, respectively.[30] X-ray photoelectron spectroscopy (XPS) was conducted

to investigate the chemical state of the SC, sulfur anion, and nickel cation. As shown in Fig. 2c, C, Ni, S, and O elements coexisted in the NiS<sub>2</sub>/SC sample. The binding states of C, Ni, and S elements were further illustrated by high-resolution spectra analysis. The C1s spectrum had two obvious peaks and a high bonding-energy peak, attributed to the C-C (284.8 eV), C-O (285.7 eV), and  $\pi$ - $\pi^*$  satellite (290.2 eV) bonds, respectively (Fig. 2d).[31] The high-resolution Ni 2p spectrum was fitted into the existing Ni<sup>2+</sup> (854.3 eV for 2p<sub>3/2</sub> and 871.9 eV for 2p<sub>1/2</sub>) and Ni<sup>3+</sup> (856.2 eV for 2p<sub>3/2</sub> and 875.1 eV 2p<sub>1/2</sub>). Additionally, two satellite peaks at 859.32 and 878.47 eV were observed, attributed to the 2p<sub>3/2</sub> and 2p<sub>1/2</sub>, respectively (Fig. 2e).[32, 33] The presence of Ni<sup>3+</sup> was due to the superficial oxidation of sulfide material when storing the NiS<sub>2</sub>/SC material in air. Oxidation caused the particular intensity of Ni<sup>3+</sup> in NiS<sub>2</sub>/SC.[34] NiS<sub>2</sub>/SC showed one pair of peaks at 162.9 and 164.0 eV, which was assigned to S<sub>2</sub><sup>2-</sup> 2p<sub>3/2</sub> and S<sub>2</sub><sup>2-</sup> 2p<sub>1/2</sub>, respectively (Fig. 2f).[18, 22] Moreover, the peak located at 169.1 eV was ascribed to the S-O covalent bond owing to the oxidation, and the obvious peak at 164.5 eV confirmed the existence of the C-S-C bond owing to the SC.[31, 33] The XPS results of NiS<sub>2</sub> and Ni/C are also exhibited in Fig. S4.

The electrochemical performance of Al pouch cells was tested to investigate the Al-ion storage capability in NiS<sub>2</sub>/SC. First, the initial five cycles of CV curves were observed to reveal the redox process of NiS<sub>2</sub>/SC at a low scan rate of 1 mV s<sup>-1</sup> (Fig. 3a) without activation. An increased reduction peak and a broad reduction peak within 0.01–1.25 V vs. Al<sup>3+</sup>/Al were observed in the initial five cycles. The corresponding

multistep oxidations had one main peak at about 1.5 V and three broad peaks that increased with the repeat scan. The slight shift of the peaks may be associated with the structural rearrangement as caused by the compositional changes.[21, 35, 36] Especially, the anodic peak near 1.7 V shifts to a higher voltage, which is probably due to the activation process with the formation of SEI or polysulfides.[37-39] NiS<sub>2</sub> without SC had a similar redox peak, but a lower reaction current. This finding indicates inferior kinetics owing to the poor electrical conductivity and inferior interfacial area with electrolyte (Fig. S5a). In good agreement with the redox behavior of CV measurement, the charge and discharge curves at a current density of 200 mA g<sup>-1</sup> ranging within 0.01–1.95 V are shown in Figs. 3b and S5b. The NiS<sub>2</sub>/SC cathode exhibited a discharge capacity of 170 mAh g<sup>-1</sup> at the first discharge with a clear slope discharge from 1.0 V to 0.01 V. In the subsequent five cycles, the electrochemical polarization decreased and the discharge capacity of 185 mAh g<sup>-1</sup> was observed at the fifth discharge. Conversely, the NiS<sub>2</sub> cathode displayed low capacity (118 mAh g<sup>-1</sup> for the first discharge and 138 mAh g<sup>-1</sup> for the fifth discharge) and poor reversibility, further confirming the necessity of the SC layer.

The other two cutoff voltages (1.8 and 2.0 V) were set to test the utilization of the cathode in the Al-ion battery system (Figs. 3c and S5c-e). Within the same voltage range, NiS<sub>2</sub>/SC demonstrated superior electrochemical capacity over NiS<sub>2</sub>. In the case of the cutoff voltage range from 0.01 to 1.95 V, even if NiS<sub>2</sub> had a higher C<sub>eff</sub>, the inefficient utilization of cathode material caused a low capacity. Low C<sub>eff</sub> and fast

capacity decay were observed with cutoff voltage ranging within 0.01–2.0 V, owing to the quick decomposition of material at a high voltage. And low capacity was observed with cutoff voltage ranging within 0.01-1.8 V, owing to the inefficient utilization of cathode material. To maintain a decent capacity and  $C_{\text{eff}}$  and stable cyclic performance, the cutoff voltage of the AIBs was preferred at 1.95 V in the following test. By considering the effect of the SC, SC without  $\text{NiS}_2$  was obtained through simple etching and sulfidation. A very small capacity was observed for the SC material, i.e., about 12  $\text{mAh g}^{-1}$ , which barely affected the acquired capacity of  $\text{NiS}_2/\text{SC}$  material (Fig. S5d).

Superior rate capability of  $\text{NiS}_2/\text{SC}$  under various current densities was also observed (Figs. 3d and 3e). An activated discharge capacity of 105  $\text{mAh g}^{-1}$  at 200  $\text{mA g}^{-1}$  was obtained, maintaining about 60  $\text{mAh g}^{-1}$  at 1000  $\text{mA g}^{-1}$ . The capacity was retained to 115  $\text{mAh g}^{-1}$  after the current density returned to 100  $\text{mA g}^{-1}$ , signifying the superior rate performance of  $\text{NiS}_2/\text{SC}$  material over  $\text{NiS}_2$  without SC (52  $\text{mAh g}^{-1}$  at 200  $\text{mA g}^{-1}$  decreased to 17  $\text{mAh g}^{-1}$  at 1000  $\text{mA g}^{-1}$ ) (Figs. S6a and S6b). Additionally, EIS was conducted on the electrode at the original and after 100 cycles from 100 kHz to 0.1 Hz with the results shown in Figs. 3f and S7. Thanks to the presence of SC, the impedance of  $R_s$  for  $\text{NiS}_2/\text{SC}$  electrode was about only 5  $\Omega$ , and the impedance of  $R_{\text{ct}}$  remarkably decreased after 100 cycles, indicating that SC can enhance the conductivity of the material and offer rapid charge transfer. The galvanostatic intermittent titration technique (GITT) was used to further assess the  $\text{Al}^{3+}$  diffusion dynamics after five-cycle activation, showing the quick discharge voltage drops (ohm drop, IR) and slow

decrease in  $\Delta E_{\tau}$  in Fig. S8a. The GITT-determined discharge/charge curves showed consistent discharge capacity (Fig. S8b and S8c), similar to the galvanostatic discharge (Figs. 3b and S5b). The  $\text{Al}^{3+}$  diffusion coefficient ( $D$ ) ranged within  $10^{-10}$  to  $10^{-13}$   $\text{cm}^2 \text{s}^{-1}$  in the intercalation process, in which the  $D$  in  $\text{NiS}_2/\text{SC}$  was mostly higher than that in  $\text{NiS}_2$  (Fig. S8d). Thus, the superior electrochemical performance of  $\text{NiS}_2/\text{SC}$  should typically be associated with the SC layer, which improved the electronic conductivity and charge transfer of  $\text{Al}^{3+}$ .

As shown in Fig. 3g, the long-cycling stability was assessed in AIBs at  $500 \text{ mA g}^{-1}$ . By using  $\text{NiS}_2/\text{SC}$ , an initial discharge capacity of  $140 \text{ mAh g}^{-1}$  was found, and a discharge capacity of  $53 \text{ mAh g}^{-1}$  remained after 500 cycles with a high and stable  $C_{\text{eff}}$  of 97%. Conversely,  $\text{NiS}_2$  showed a low initial discharge capacity of  $85 \text{ mAh g}^{-1}$ , and the discharge capacity dropped to  $20 \text{ mAh g}^{-1}$  after 500 cycles (Fig. S9). Results showed that  $\text{NiS}_2/\text{SC}$  material had better cycling stability and higher capacity than  $\text{NiS}_2$  material. To elucidate the capacity fading of  $\text{NiS}_2/\text{SC}$  and  $\text{NiS}_2$  in the first 50 cycles, SEM and TEM analyses were conducted to further characterize the morphology of  $\text{NiS}_2/\text{SC}$  material after 100 cycles (Fig. 3h). Numerous holes were observed at the particles and some  $\text{NiS}_2$  particles disappeared from the embraced carbon layer owing to the structure pulverization with the repeat intercalation/deintercalation of Al ion into the interior  $\text{NiS}_2$  structure and the dissolution and loss of intermediate products. Nevertheless, the  $\text{NiS}_2$  particles exhibited uniform distribution without particle agglomeration owing to the protection of the carbon layer. After cycling, the

pulverization and agglomeration of NiS<sub>2</sub> were observed and found to decrease electrochemical performance (Fig. S10). Thus, the energy-storage and capacity-deterioration mechanisms of NiS<sub>2</sub>/SC cathode material urgently need to be revealed to further improve electrochemical ability.

To gain insights into the Al<sup>3+</sup> storage mechanism in NiS<sub>2</sub>/SC electrode, a series of *ex situ* investigations including XRD, XPS, UV, and TEM were performed after a five-cycle activation process. The electrode samples for the *ex situ* studies were collected at different voltage stages (Fig. 4a). As shown in Fig. 4b, at the full-discharge state (0.01 V), the characteristic XRD pattern for NiS<sub>2</sub>/SC at 2-theta of 20 –50° had a clear decrease in peak intensity and retained only the obvious (200) peak at 31.5°. The reduced peak intensity was ascribed to the low crystallinity or amorphous product caused by the rearrangement of the lattice after the Al<sup>3+</sup> insertion.[17] At the full charge state, the diffraction peaks of the NiS<sub>2</sub> phase were recovered, indicating reversible electrochemical reactions of NiS<sub>2</sub>/SC in the Al-ion battery at the first few cycles. The (200) peak showed a slight shift to a lower angle at the full discharge state and recovered at the full charge state, indicating negligible volume change during the electrochemical intercalation/deintercalation of Al<sup>3+</sup>. Notably, the peak at 2-theta of 40.6° was attributed to the molybdenum current collector. For gain the detailed information on material structural evolution during cycling, We provided the in situ XRD of the 1<sup>st</sup> discharge/charge and 2<sup>nd</sup> discharge processes in the revised manuscript (Fig. S11). As shown in Fig. S11, a clear decrease of (111) peak intensity was observed during the

discharging process and the complete disappearance of the (111) peak intensity at the full-discharge state (0.01 V). And these peaks were partially recovered during the charging process. The obvious (002) peak at  $31.5^\circ$  showed a slight shift to a lower angle during the discharging process, which indicates a minor expansion of the lattice parameter after  $\text{Al}^{3+}$  insertion. At the same time, the (002) peak recovered back during the charging process. Additionally, all peak intensity at the full-discharge state (0.01 V) is lower than that at the full-charge state (1.95 V) which is ascribed to the low crystallinity or amorphous product caused by the rearrangement of the lattice after the  $\text{Al}^{3+}$  insertion. These results indicate the reversible electrochemical reactions of  $\text{NiS}_2/\text{SC}$  in the Al-ion battery at the first few cycles. The in situ XRD results are in good agreement with the ex situ XRD results in the manuscript (Fig. 4b). Considering the poor crystallinity, TEM analysis was further performed to investigate its phase components. Amorphous products were confirmed on the surface of  $\text{NiS}_2$  with a large area after the full discharge (Fig. 4c). Furthermore,  $\text{NiS}_2$  partially recovered after the full charge with some amorphous phases owing to the existence of the trapped Al ion in the  $\text{NiS}_2$  structure (Fig. 4d).

XPS analyses were conducted at various potentials to monitor the change in oxidation state and the chemical composition of S, Al, Cl, and Ni elements during the Al-ion uptake and removal.[22] All XPS samples after the electrochemical process were prepared in a glove box and transferred into a special chamber under an argon atmosphere without exposure to the air to reduce contamination (Fig. S12). The etching

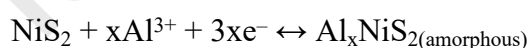
XPS analysis was utilized for NiS<sub>2</sub>/SC and showed that after 60 s etching time, the atomic percentage of the C1s, S2p, and Ni2p remained the same with further increasing etch time beyond 60 s, indicating that the surface carbon layer was etched after 60 s etching time (Fig. S13). So their XPS patterns were collected after a 60s etch time to etch the surface carbon layer and explain the anionic redox process. As shown in the S 2p detail spectra (Fig. 4e), the pristine NiS<sub>2</sub>/SC demonstrated two characteristic peaks at binding energies of 162.9 eV (S<sub>2</sub><sup>2-</sup> 2p<sub>3/2</sub>) and 164.0 eV (S<sub>2</sub><sup>2-</sup> 2p<sub>1/2</sub>), corresponding with the doublet peaks of the S<sub>2</sub><sup>2-</sup> dimer. All spectra were fitted with the spin-orbit splitting energy of 1.16 eV and intensity ratio of 0.5 between the S<sub>2</sub><sup>2-</sup> 2p<sub>3/2</sub> and S<sub>2</sub><sup>2-</sup> 2p<sub>1/2</sub> peak. At the beginning discharge to 0.6 V, in the S 2p spectrum, two pairs of peaks with different S 2p<sub>3/2</sub> binding energies of 162.1 and 163.4 eV were observed, which were assigned to the S<sup>2-</sup> and S<sub>n</sub><sup>2-</sup> (2 ≤ n < 8) ions (S<sub>n</sub><sup>2-</sup> including S<sub>2</sub><sup>2-</sup> and some polysulfides on the surface and in the subsurface region), respectively.[21, 22] This process was similar to the evolution of a series of polysulfides in Al-S batteries and some TMSs.[3, 20, 40] The S<sup>2-</sup> peak demonstrated the reduction from S<sub>2</sub><sup>2-</sup> dimers, and S<sub>n</sub><sup>2-</sup> indicated the oxidation of S<sub>2</sub><sup>2-</sup> dimers probably owing to the previous activation process. At the full discharge, the broad S<sub>n</sub><sup>2-</sup> peaks gradually decreased, whereas the position of the S<sup>2-</sup> peaks remained constant with increased peak intensity. When being charged, the S<sup>2-</sup> peak intensity decreased and the S<sub>n</sub><sup>2-</sup> peak gradually increased and broadened with the excessive oxidation, indicating that the sulfur at the center caused the redox reactions during the Al<sup>3+</sup> deintercalation. The variations in the S<sup>2-</sup> 2p<sub>3/2</sub>/S<sub>n</sub><sup>2-</sup> 2p<sub>3/2</sub> peak ratio were 0.86 at discharged 0.6 V, 1.16 at discharged 0.01 V, 0.83 at charged 1.6 V, and 0.73 at

charged 1.95 V respectively. The  $S_n^{2-}$  2p<sub>3/2</sub> peak was centered at 163.4 eV, which positively shifted by 0.5 eV from the corresponding 2p<sub>3/2</sub> peak of NiS<sub>2</sub>/SC, suggesting the existence of some polysulfides and the partial reversibility of NiS<sub>2</sub>/SC at the full charge. The high ratio of S<sup>2-</sup> peak intensity during the process was possibly due to the residual Al<sup>3+</sup> trapping in the structure. The chemical state of Ni cation in NiS<sub>2</sub>/SC was analyzed by the Ni 2p XPS spectra (Fig. S14a). The positions of the Ni 2p peaks showed no observable changes during the cycling. However, all positions of Ni 2p<sub>3/2</sub> and 2p<sub>1/2</sub> during the cycling shifted to lower binding energies of 853.8 and 870.9 eV, respectively, with respect to the original NiS<sub>2</sub>/SC materials, indicating the concomitant cationic redox owing to the reduction of the original Ni after the initial activation. Fig. S14b shows the XPS spectra of Al 2p and Cl 2p at the full charge and the full discharge. The peak position of Al 2p slightly positively shifted after the discharge compared with the peak at the charged state, which was possible due to the trapped Al ion in the inner structure of NiS<sub>2</sub>/SC. However, no obvious change occurred in the peak intensity and the position of Cl 2p. The XPS results confirmed that after the Al-ion insertion, S<sub>2</sub><sup>2-</sup> was reduced to S<sup>2-</sup>, accompanying with the reduction of Ni<sup>2+</sup>. Subsequently, during the cycling, S<sup>2-</sup> was partially reversed to S<sub>2</sub><sup>2-</sup> as the main anionic redox centers, and the reduced Ni state was observed owing to the existence of trapped Al in the surface structure.

To further elucidate the transformation of polysulfides during the cycling, *ex situ* UV analysis was performed for the electrolyte at various voltage stages (Fig. 4f).[41]

In the charged process, the peak intensity at 350 and 464 nm gradually increased and almost disappeared at the full-discharge state, indicating the high dissolution of polysulfides at high charge voltage and a partially reversible redox reaction of sulfur in ionic-liquid electrolyte. Raman spectra were obtained to characterize the structural information of the liquid electrolyte (Fig. S15). The fresh electrolyte had a small peak at 311  $\text{cm}^{-1}$ , a strong peak at 350  $\text{cm}^{-1}$ , and another peak at 596  $\text{cm}^{-1}$ , attributed to  $\text{Al}_2\text{Cl}_7^-$ ,  $\text{AlCl}_4^-$ , and  $\text{EMI}^+$ , respectively.  $\text{Al}_2\text{Cl}_7^-$  decomposed into  $\text{AlCl}_4^-$  during the charging, and the characteristic peak weakened. The low peak intensity including that of the  $\text{AlCl}_4^-$  ion was due to the disturbance of the polysulfide ion in the electrolyte. In the process of discharge, the reaction of Al with  $\text{AlCl}_4^-$  ions was conducted to form  $\text{Al}_2\text{Cl}_7^-$  ions.

Based on the above measurements, the mechanism of the Al-ion storage in  $\text{NiS}_2/\text{SC}$  can be tentatively proposed as follows (Fig. 4g):



During the discharge, Al inserted into the  $\text{NiS}_2$  lattice structure to form amorphous  $\text{Al}_x\text{NiS}_2$  phase with the sulfur anions acting as the main redox centers and the partial reduction of  $\text{Ni}^{2+}$  to  $\text{Ni}^{4-3x}$  ( $2/3 < x < 4/3$ ) cations occurring to achieve local electroneutrality. During the charge,  $\text{S}^{2-}$  was oxidized to  $\text{S}_2^{2-}$ , and even some parts were oxidized to polysulfides in high charge voltage with Al-ion extraction. The main reasons for the capacity decay and deterioration mechanisms of the  $\text{NiS}_2/\text{SC}$  cathode material during the  $\text{Al}^{3+}$  intercalation/deintercalation was the loss of the active phase,

i.e., (1) during discharge, Al ions inserted and destroyed the crystal  $\text{NiS}_2$  to form amorphous  $\text{Al}_x\text{NiS}_2$  and were trapped in the structure at the following charge process; and (2) during charge, the sulfur anions as the main redox centers were overoxidized to polysulfides, which substantially dissolved in the electrolyte.

Based on the above analysis of the capacity-deterioration mechanism, we proposed the utilization of SC nanofiber (SCNF) as a wrapping and conductive layer to further optimize the  $\text{NiS}_2/\text{SC}$  cathode. SCNF was conducive to avoiding the loss of polysulfides and increasing the conductivity of the active material to reduce the trapped Al ion.[31, 42-44] With this purpose, Ni/SC was combined with electrospinning to form the Ni/SC@PAN, followed by simple calcination and sulfidation process to obtain the  $\text{NiS}_2/\text{SC}@SCNF$ . The schematic of the as-prepared Al-ion battery with the  $\text{NiS}_2/\text{SC}@SCNF$  cathode is shown in Fig. 5a. The successful combination of  $\text{NiS}_2/\text{SC}$  and SCNF can be confirmed through SEM and TEM analyses (Figs. 5b and 5c). The electrode showed a uniform carbon nanofiber only with some particles outside the fiber, owing to the breakage of the thin fiber. HRTEM images were also acquired to gain deep insights into the  $\text{NiS}_2/\text{SC}@SCNF$  structure. Results showed that  $\text{NiS}_2/\text{SC}$  was well encapsulated in the SC nanofibers, and the corresponding elemental mapping images (Ni, S, and C) of  $\text{NiS}_2/\text{SC}@SCNF$  further confirmed that the active material was dispersed in the fiber interior. The XRD pattern of  $\text{NiS}_2/\text{SC}@SCNF$  showed the typical peaks of the cubic  $\text{NiS}_2$  phase, which had no obvious difference from the peaks of  $\text{NiS}_2/\text{SC}$  (Fig. S16a). TGA test results confirmed 42.1% mass percentage of active

materials and 57.9% mass percentage of carbon in NiS<sub>2</sub>/SC@SCNF owing to the co-existence of SCNF (Fig. S16b). Consequently, the electrochemical performance of the NiS<sub>2</sub>/SC@SCNF electrode displayed a similar charge and discharge curve to the NiS<sub>2</sub>/SC electrode and was barely affected by the pure SCNF regarding the obtained capacity (Fig. 5d). After a slow initial capacity decay, a specific discharge capacity of 82 mAh g<sup>-1</sup> was achieved after 100 cycles at 200 mA g<sup>-1</sup> (Fig. S17). To investigate the dissolution of polysulfides in NiS<sub>2</sub>/SC and NiS<sub>2</sub>/SC@SCNF after the cycling, UV studies were performed on the electrolytes after 200 cycles at 200 mA g<sup>-1</sup> current density (Fig. 5e). The electrolyte with NiS<sub>2</sub>/SC@SCNF had a lighter color than that with NiS<sub>2</sub>/SC from the optical photograph, indicating that fewer polysulfide ions were dissolved in electrolytes (Fig. 5e insert). Meanwhile, the UV spectra of electrolyte with NiS<sub>2</sub>/SC showed a larger absorption peak at 464 nm than that of electrolyte with NiS<sub>2</sub>/SC@SCNF, indicating that encapsulating the NiS<sub>2</sub>/SC in SCNF structure can effectively avoid the loss of polysulfides and resulted in superior electrochemical performance. The NiS<sub>2</sub>/SC@SCNF cathode showed outstanding cycling performance, with a significantly slower capacity-loss rate and a discharge capacity of 76 mAh g<sup>-1</sup> after 500 cycles with a coulombic efficiency of 97%, indicating that the presence of SCNF could promote cycling stability (Fig. 5f). The decent rate capability of NiS<sub>2</sub>/SC@SCNF under various current densities was also observed (Fig. S18). Thus, the exterior of SCNF formed a barrier that retarded the loss of polysulfides to the electrolyte and served as a three-dimensional interconnected conductive network facilitating electron transport, thereby causing high stability and performance during

repeat cycling, compared with previously typical metal sulfide cathode materials for AIBs (Table S1).

#### 4. Conclusion

We have prepared and investigated NiS<sub>2</sub>/SC as cathode for AIBs. The anionic redox-reaction mechanism of S<sub>2</sub><sup>2-</sup> to S<sup>2-</sup> of NiS<sub>2</sub>-based cathode was proposed and fully analyzed. A series of measurements revealed that NiS<sub>2</sub>/SC underwent a reversible evolution of initial Al<sup>3+</sup> insertion followed by anionic redox between S<sub>2</sub><sup>2-</sup> and S<sup>2-</sup>. In particular, it was found that the Al-ion storage in NiS<sub>2</sub>/SC was likely via the route as follows: NiS<sub>2</sub> + xAl<sup>3+</sup> + 3xe<sup>-</sup> ↔ Al<sub>x</sub>NiS<sub>2(amorphous)</sub>. The anionic redox-reaction mechanism of NiS<sub>2</sub>-based cathode elucidated the electrochemical behavior of the special Ni-based sulfide electrodes in the Al-ion battery system. To further improve the electrode performance for Al storage, we successfully prepared a new class of electrospun NiS<sub>2</sub>/SC@SCNF cathode for AIBs. The cathode had superior stable electrochemical performance (discharge capacity of 82 mAh g<sup>-1</sup> at 200 mA g<sup>-1</sup> after 100 cycles and 76 mAh g<sup>-1</sup> at 500 mA g<sup>-1</sup> after 500 cycles). The results were significantly meaningful for understanding the capacity-storage mechanism of NiS<sub>2</sub>-based cathode materials for the future development of aluminum-ion storage.

#### Acknowledgements

This work was funded by the Science and Technology Development Fund, Macau SAR (File no. 0191/2017/A3, 0041/2019/A1, 0046/2019/AFJ, 0021/2019/AIR, 0007/2021/AGJ), University of Macau (File no. MYRG2017-00216-FST, MYRG2018-00192-IAPME, MYRG2020-00187-IAPME), the UEA funding, Science

and Technology Program of Guangzhou (2019050001), and National Key Research and Development Program of China (2019YFE0198000). F. Chen acknowledges the Pearl River Talent Program (2019QN01L951).

**Competing financial interests**

The authors declare no competing financial interests

**References**

- [1] J. Tu, W.-L. Song, H. Lei, Z. Yu, L.-L. Chen, M. Wang, S. Jiao, Nonaqueous Rechargeable Aluminum Batteries: Progresses, Challenges, and Perspectives, *Chem. Rev.* 121 (8) (2021) 4903-4961, <https://doi.org/10.1021/acs.chemrev.0c01257>.
- [2] E. Faegh, B. Ng, D. Hayman, W. E. Mustain, Practical assessment of the performance of aluminium battery technologies, *Nat. Energy* 6 (1) (2021) 21-29, <https://doi.org/10.1038/s41560-020-00728-y>.
- [3] S. He, D. Zhang, X. Zhang, S. Liu, W. Chu, H. Yu, Rechargeable Al-Chalcogen Batteries: Status, Challenges, and Perspectives, *Adv. Energy Mater.* 11 (29) (2021) 2100769, <https://doi.org/10.1002/aenm.202100769>.
- [4] H. Wang, L. Zhao, H. Zhang, Y. Liu, L. Yang, F. Li, W. Liu, X. Dong, X. Li, Z. Li, X. Qi, L. Wu, Y. Xu, Y. Wang, K. Wang, H. Yang, Q. Li, S. Yan, X. Zhang, F. Li, H. Li, Revealing the multiple cathodic and anodic involved charge storage mechanism in an FeSe<sub>2</sub> cathode for aluminium-ion batteries by in situ magnetometry, *Energy Environ. Sci.* 15 (1) (2022) 311-319, <https://doi.org/10.1039/D1EE03070A>.
- [5] H. Zhang, Y. Liu, L. Yang, L. Zhao, X. Dong, H. Wang, Y. Li, T. Sun, Q. Li, H. Li, Evidence for dual anions co-insertion in a transition metal chalcogenide cathode material NiSe<sub>2</sub> for high-performance rechargeable aluminum-ion batteries, *Energy Stor. Mater.* 47 (2022) 336-344, <https://doi.org/10.1016/j.ensm.2022.02.026>.
- [6] H. Yang, H. Li, J. Li, Z. Sun, K. He, H.-M. Cheng, F. Li, The Rechargeable Aluminum Battery: Opportunities and Challenges, *Angew.Chem.Int. Ed.* 58 (35) (2019) 11978–11996, <https://doi.org/10.1002/anie.201814031>.

- [7] Z. Rong, R. Malik, P. Canepa, G. Sai Gautam, M. Liu, A. Jain, K. Persson, G. Ceder, Materials Design Rules for Multivalent Ion Mobility in Intercalation Structures, *Chem. Mater.* 27 (17) (2015) 6016-6021, <https://doi.org/10.1021/acs.chemmater.5b02342>.
- [8] L. Geng, J. P. Scheifers, C. Fu, J. Zhang, B. P. Fokwa, J. Guo, Titanium sulfides as intercalation-type cathode materials for rechargeable aluminum batteries, *ACS Appl. Mater. Interfaces* 9 (25) (2017) 21251-21257, <https://doi.org/10.1021/acsami.7b04161>.
- [9] Y. Tong, A. Gao, Q. Zhang, T. Gao, J. Yue, F. Meng, Y. Gong, S. Xi, Z. Lin, M. Mao, S. Peng, X. Wang, D. Xiao, D. Su, Y. Luo, H. Li, L. Chen, L. Suo, L. Gu, Cation-synergy stabilizing anion redox of Chevrel phase  $\text{Mo}_6\text{S}_8$  in aluminum ion battery, *Energy Stor. Mater.* 37 (2021) 87-93, <https://doi.org/10.1016/j.ensm.2021.01.033>.
- [10] F. Wu, H. Yang, Y. Bai, C. Wu, Paving the Path toward Reliable Cathode Materials for Aluminum-Ion Batteries, *Adv. Mater.* 31 (16) (2019) 1806510, <https://doi.org/10.1002/adma.201806510>.
- [11] Z. Yu, Z. Kang, Z. Hu, J. Lu, Z. Zhou, S. Jiao, Hexagonal NiS nanobelts as advanced cathode materials for rechargeable Al-ion batteries, *Chem. Commun.* 52 (68) (2016) 10427-10430, <https://doi.org/10.1039/C6CC05974K>.
- [12] S. Wang, Z. Yu, J. Tu, J. Wang, D. Tian, Y. Liu, S. Jiao, A Novel Aluminum-Ion Battery:  $\text{Al}/\text{AlCl}_3\text{-[EMIm] Cl}/\text{Ni}_3\text{S}_2@ \text{Graphene}$ , *Adv. Energy Mater.* 6 (13) (2016) 1600137, <https://doi.org/10.1002/aenm.201600137>.
- [13] S. Wang, S. Jiao, J. Wang, H.-S. Chen, D. Tian, H. Lei, D.-N. Fang, High-

performance aluminum-ion battery with CuS@ C microsphere composite cathode, ACS Nano 11 (1) (2016) 469–477, <https://doi.org/10.1021/acsnano.6b06446>.

[14] Y. Hu, B. Luo, D. Ye, X. Zhu, M. Lyu, L. Wang, An Innovative Freeze-Dried Reduced Graphene Oxide Supported SnS<sub>2</sub> Cathode Active Material for Aluminum-Ion Batteries, Adv. Mater. 29 (48) (2017) 1606132, <https://doi.org/10.1002/adma.201606132>.

[15] Z. Zhao, Z. Hu, Q. Li, H. Li, X. Zhang, Y. Zhuang, F. Wang, G. Yu, Designing two-dimensional WS<sub>2</sub> layered cathode for high-performance aluminum-ion batteries: From micro-assemblies to insertion mechanism, Nano Today 32 (2020) 100870, <https://doi.org/10.1016/j.nantod.2020.100870>.

[16] E. D. Grayfer, E. M. Pazhetnov, M. N. Kozlova, S. B. Artemkina, V. E. Fedorov, Anionic Redox Chemistry in Polysulfide Electrode Materials for Rechargeable Batteries, ChemSusChem 10 (24) (2017) 4805-4811, <https://doi.org/10.1002/cssc.201701709>.

[17] T. Mori, Y. Orikasa, K. Nakanishi, C. Kezheng, M. Hattori, T. Ohta, Y. J. J. o. P. S. Uchimoto, Discharge/charge reaction mechanisms of FeS<sub>2</sub> cathode material for aluminum rechargeable batteries at 55° C, J. Power Sources 313 (2016) 9-14, <https://doi.org/10.1016/j.jpowsour.2016.02.062>.

[18] Z. Lin, M. Mao, C. Yang, Y. Tong, Q. Li, J. Yue, G. Yang, Q. Zhang, L. Hong, X. Yu, L. Gu, Y.-S. Hu, H. Li, X. Huang, L. Suo, L. Chen, Amorphous anion-rich titanium polysulfides for aluminum-ion batteries, Sci. Adv. 7 (35) (2021) eabg6314, <https://doi.org/10.1126/sciadv.abg6314>.

- [19] M. Mao, Y. Tong, Q. Zhang, Y.-S. Hu, H. Li, X. Huang, L. Chen, L. Gu, L. Suo, Joint Cationic and Anionic Redox Chemistry for Advanced Mg Batteries, *Nano Lett.* 20 (9) (2020) 6852-6858, <https://doi.org/10.1021/acs.nanolett.0c02908>.
- [20] Z. Wang, X. Li, W. Guo, Y. Fu, Anion Intercalation of VS<sub>4</sub> Triggers Atomic Sulfur Transfer to Organic Disulfide in Rechargeable Lithium Battery, *Adv. Funct. Mater.* 31 (16) (2021) 2009875, <https://doi.org/10.1002/adfm.202009875>.
- [21] Z. Li, B. P. Vinayan, P. Jankowski, C. Njel, A. Roy, T. Vegge, J. Maibach, J. M. G. Lastra, M. Fichtner, Z. Zhao-Karger, Multi-Electron Reactions Enabled by Anion-Based Redox Chemistry for High-Energy Multivalent Rechargeable Batteries, *Angew. Chem. Int. Ed.* 59 (28) (2020) 11483-11490, <https://doi.org/10.1002/anie.202002560>.
- [22] S. Dey, J. Lee, S. Britto, J. M. Stratford, E. N. Keyzer, M. T. Dunstan, G. Cibin, S. J. Cassidy, M. Elgaml, C. P. Grey, Exploring Cation–Anion Redox Processes in One-Dimensional Linear Chain Vanadium Tetrasulfide Rechargeable Magnesium Ion Cathodes, *J. Am. Chem. Soc.* 142 (46) (2020) 19588-19601, <https://doi.org/10.1021/jacs.0c08222>.
- [23] G. Zhao, Y. Zhang, L. Yang, Y. Jiang, Y. Zhang, W. Hong, Y. Tian, H. Zhao, J. Hu, L. Zhou, Nickel chelate derived NiS<sub>2</sub> decorated with bifunctional carbon: an efficient strategy to promote sodium storage performance, *Adv. Funct. Mater.* 28 (41) (2018) 1803690, <https://doi.org/10.1002/adfm.201803690>.
- [24] Y. Zhang, F. Lu, L. Pan, Y. Xu, Y. Yang, Y. Bando, D. Golberg, J. Yao, X. Wang, Improved cycling stability of NiS<sub>2</sub> cathodes through designing a “kiwano”

- hollow structure, *J. Mater. Chem. A* 6 (25) (2018) 11978-11984, <https://doi.org/10.1039/C8TA01551A>.
- [25] J. Li, J. Li, D. Yan, S. Hou, X. Xu, T. Lu, Y. Yao, W. Mai, L. Pan, Design of pomegranate-like clusters with NiS<sub>2</sub> nanoparticles anchored on nitrogen-doped porous carbon for improved sodium ion storage performance, *J. Mater. Chem. A* 6 (15) (2018) 6595-6605, <https://doi.org/10.1039/C8TA00557E>.
- [26] J. Rouxel, Anion–Cation Redox Competition and the Formation of New Compounds in Highly Covalent Systems, *Chem. Eur. J.* 2 (9) (1996) 1053-1059, <https://doi.org/10.1002/chem.19960020904>.
- [27] J. Rouxel, Some solid state chemistry with holes: Anion–cation redox competition in solids, *Curr. Sci.* 73 (1) (1997) 31-39.
- [28] S. Wang, S. Jiao, D. Tian, H. S. Chen, H. Jiao, J. Tu, Y. Liu, D. N. Fang, A Novel Ultrafast Rechargeable Multi-Ions Battery, *Adv. Mater.* 29 (16) (2017) 1606349, <https://doi.org/10.1002/adma.201606349>.
- [29] Y. Wen, K. He, Y. Zhu, F. Han, Y. Xu, I. Matsuda, Y. Ishii, J. Cumings, C. Wang, Expanded graphite as superior anode for sodium-ion batteries, *Nat. Commun.* 5 (1) (2014) 4033, <https://doi.org/10.1038/ncomms5033>.
- [30] M. C. Shin, J. H. Kim, S. Nam, Y. J. Oh, H. J. Jin, C. R. Park, Q. Zhang, S. J. Yang, Atomic-Distributed Coordination State of Metal-Phenolic Compounds Enabled Low Temperature Graphitization for High-Performance Multioriented Graphite Anode, *Small* 16 (33) (2020) 2003104, <https://doi.org/10.1002/sml.202003104>.
- [31] D. Li, L. Dai, X. Ren, F. Ji, Q. Sun, Y. Zhang, L. Ci, Foldable potassium-ion

batteries enabled by free-standing and flexible SnS<sub>2</sub>@C nanofibers, *Energy Environ. Sci.* 14 (2021) 424-436, <https://doi.org/10.1039/D0EE02919J>.

[32] D. D. Yang, M. Zhao, R. D. Zhang, Y. Zhang, C. C. Yang, Q. Jiang, NiS<sub>2</sub> nanoparticles anchored on open carbon nanohelmets as an advanced anode for lithium-ion batteries, *Nanoscale Adv.* 2 (1) (2020) 512-519, <https://doi.org/10.1039/C9NA00661C>.

[33] X. Yao, H. Cheng, Z. Jiang, Q. Han, Y. Wang, S. Wang, Heterostructured CoS<sub>2</sub>/NiS<sub>2</sub> nanoparticles encapsulated in bamboo-like carbon nanotubes as a high performance anode for sodium ion batteries, *New J. Chem.* 44 (25) (2020) 10404-10409, <https://doi.org/10.1039/D0NJ00941E>.

[34] K. N. Dinh, Y. Sun, Z. Pei, Z. Yuan, A. Suwardi, Q. Huang, X. Liao, Z. Wang, Y. Chen, Q. Yan, Electronic Modulation of Nickel Disulfide toward Efficient Water Electrolysis, *Small* 16 (17) (2020) 1905885, <https://doi.org/10.1002/smll.201905885>.

[35] Y. Shen, Q. Zhang, Y. Wang, L. Gu, X. Zhao, X. Shen, A Pyrite Iron Disulfide Cathode with a Copper Current Collector for High-Energy Reversible Magnesium-Ion Storage, *Adv. Mater.* 33 (41) (2021) 2103881, <https://doi.org/10.1002/adma.202103881>.

[36] Y. Zhou, J. Tian, H. Xu, J. Yang, Y. Qian, VS<sub>4</sub> nanoparticles rooted by a-C coated MWCNTs as an advanced anode material in lithium ion batteries, *Energy Stor. Mater.* 6 (2017) 149-156, <https://doi.org/10.1016/j.ensm.2016.10.010>.

[37] Y. Hu, H. Huang, D. Yu, X. Wang, L. Li, H. Hu, X. Zhu, S. Peng, L. Wang, All-Climate Aluminum-Ion Batteries Based on Binder-Free MOF-Derived

FeS<sub>2</sub>@C/CNT Cathode, Nano-Micro Letters 13 (1) (2021) 159,  
<https://doi.org/10.1007/s40820-021-00682-8>.

[38] Z. Ye, P. Li, W. Wei, C. Huang, L. Mi, J. Zhang, J. Zhang, In Situ Anchoring Anion-Rich and Multi-Cavity NiS<sub>2</sub> Nanoparticles on NCNTs for Advanced Magnesium-Ion Batteries, Adv. Sci. (2022) e2200067,  
<https://doi.org/10.1002/advs.202200067>.

[39] Y. Wang, Y. Zhang, J. Shi, X. Kong, X. Cao, S. Liang, G. Cao, A. Pan, Tin sulfide nanoparticles embedded in sulfur and nitrogen dual-doped mesoporous carbon fibers as high-performance anodes with battery-capacitive sodium storage, Energy Storage Materials 18 (2019) 366-374.

[40] X. Yu, A. Manthiram, Electrochemical Energy Storage with a Reversible Nonaqueous Room-Temperature Aluminum–Sulfur Chemistry, Adv. Energy Mater. 7 (18) (2017) 1700561, <https://doi.org/10.1002/aenm.201700561>.

[41] Q. Zou, Y.-C. Lu, Solvent-Dictated Lithium Sulfur Redox Reactions: An Operando UV–vis Spectroscopic Study, J. Phys. Chem. Lett. 7 (8) (2016) 1518-1525,  
<https://doi.org/10.1021/acs.jpcclett.6b00228>.

[42] S. Shi, Z. Li, L. Shen, X. Yin, Y. Liu, G. Chang, J. Wang, S. Xu, J. Zhang, Y. Zhao, Electrospun free-standing FeP@NPC film for flexible sodium ion batteries with remarkable cycling stability, Energy Stor. Mater. 29 (2020) 78-83,  
<https://doi.org/10.1016/j.ensm.2020.03.029>.

[43] X. Li, W. Chen, Q. Qian, H. Huang, Y. Chen, Z. Wang, Q. Chen, J. Yang, J. Li, Y. W. Mai, Electrospinning-Based Strategies for Battery Materials, Adv. Energy Mater.

11 (2) (2020) 2000845, <https://doi.org/10.1002/aenm.202000845>.

[44] J. Xia, L. Liu, S. Jamil, J. Xie, H. Yan, Y. Yuan, Y. Zhang, S. Nie, J. Pan, X. Wang, Free-standing SnS/C nanofiber anodes for ultralong cycle-life lithium-ion batteries and sodium-ion batteries, *Energy Stor. Mater.* 17 (2019) 1-11, <https://doi.org/10.1016/j.ensm.2018.08.005>.

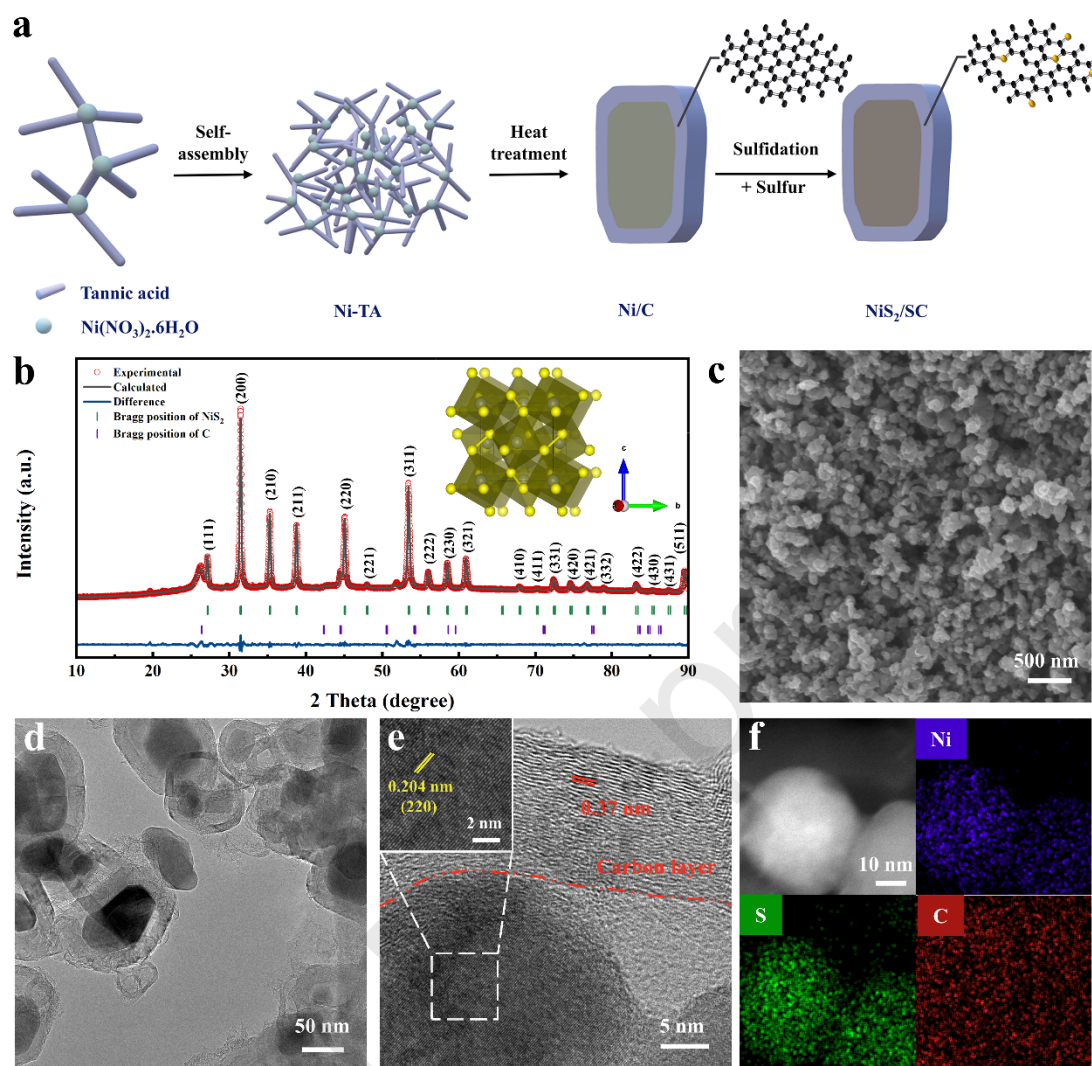


**Figure 1.** (a) Schematic of the synthesis of NiS<sub>2</sub>/S-doped carbon (NiS<sub>2</sub>/SC) material. (b) XRD pattern and its Rietveld refinement of NiS<sub>2</sub>/SC ( $R_p$  9.50%,  $R_{wp}$  7.02%,  $\chi^2 = 3.72$ ). (c) SEM image, (d) TEM image, (e) HRTEM image, and (f) corresponding element mapping (Ni, S, and C) of NiS<sub>2</sub>/SC material.

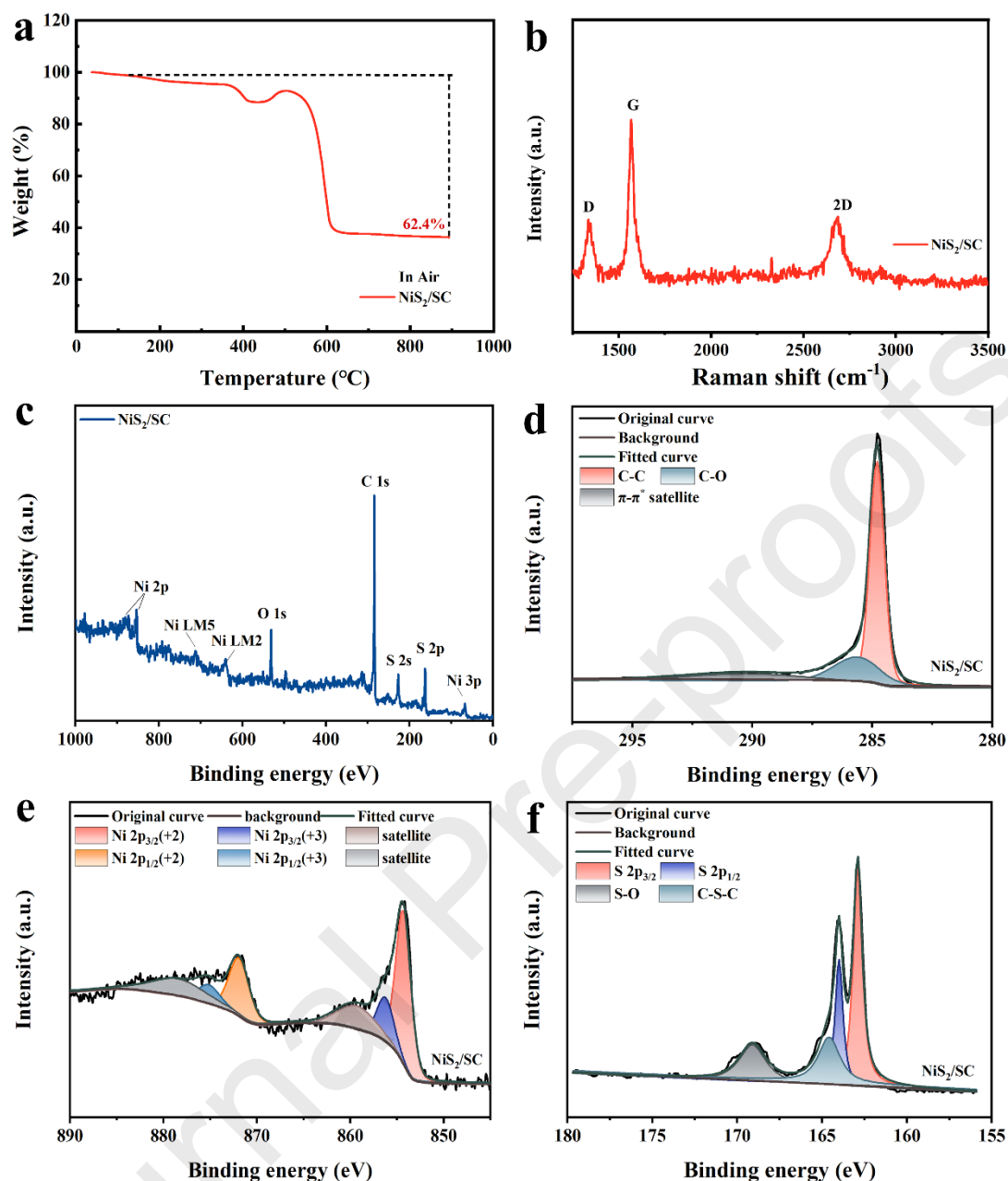


**Figure 2.** Physical and chemical information of NiS<sub>2</sub>/SC material. (a) TGA curves (mass% of NiS<sub>2</sub>/SC = 61.8%). (b) Raman spectra. (c) XPS survey spectrum. Corresponding high-resolution spectrum of (d) C 1s, (e) Ni 2p, and (f) S 2p.

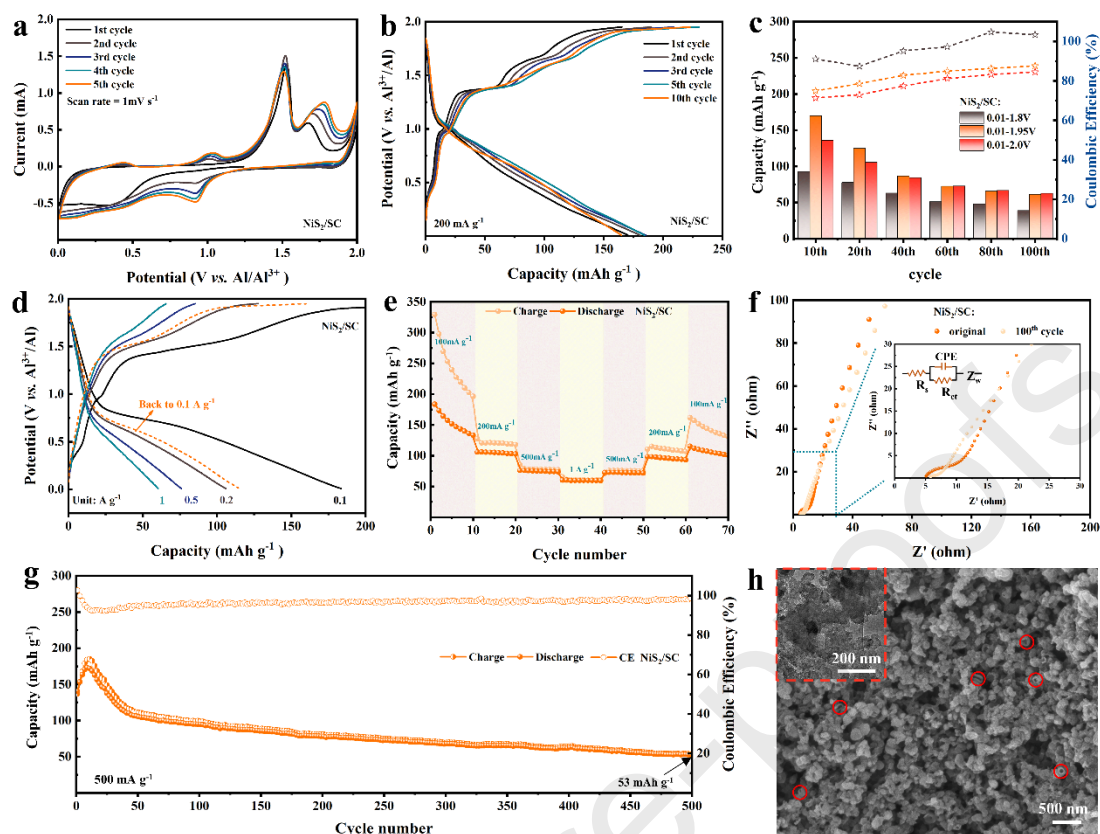


**Figure 3.** Electrochemical performance of NiS<sub>2</sub>/SC material. (a) CV curves at 1 mV s<sup>-1</sup>. (b) Galvanostatic charge and discharge curves at 200 mA g<sup>-1</sup>. (c) Cycling performance at different cutoff voltages. (d and e) Rate performance from 100 mA g<sup>-1</sup> to 1000 mA g<sup>-1</sup>. (f) Nyquist plots (insert: high-frequency region of Nyquist plots and equivalent circuit model). (g) Cycling performance and corresponding C<sub>eff</sub> at a current density of 500 mA g<sup>-1</sup>. (h) SEM and HRTEM results at the 100th cycle at 200 mA g<sup>-1</sup>.

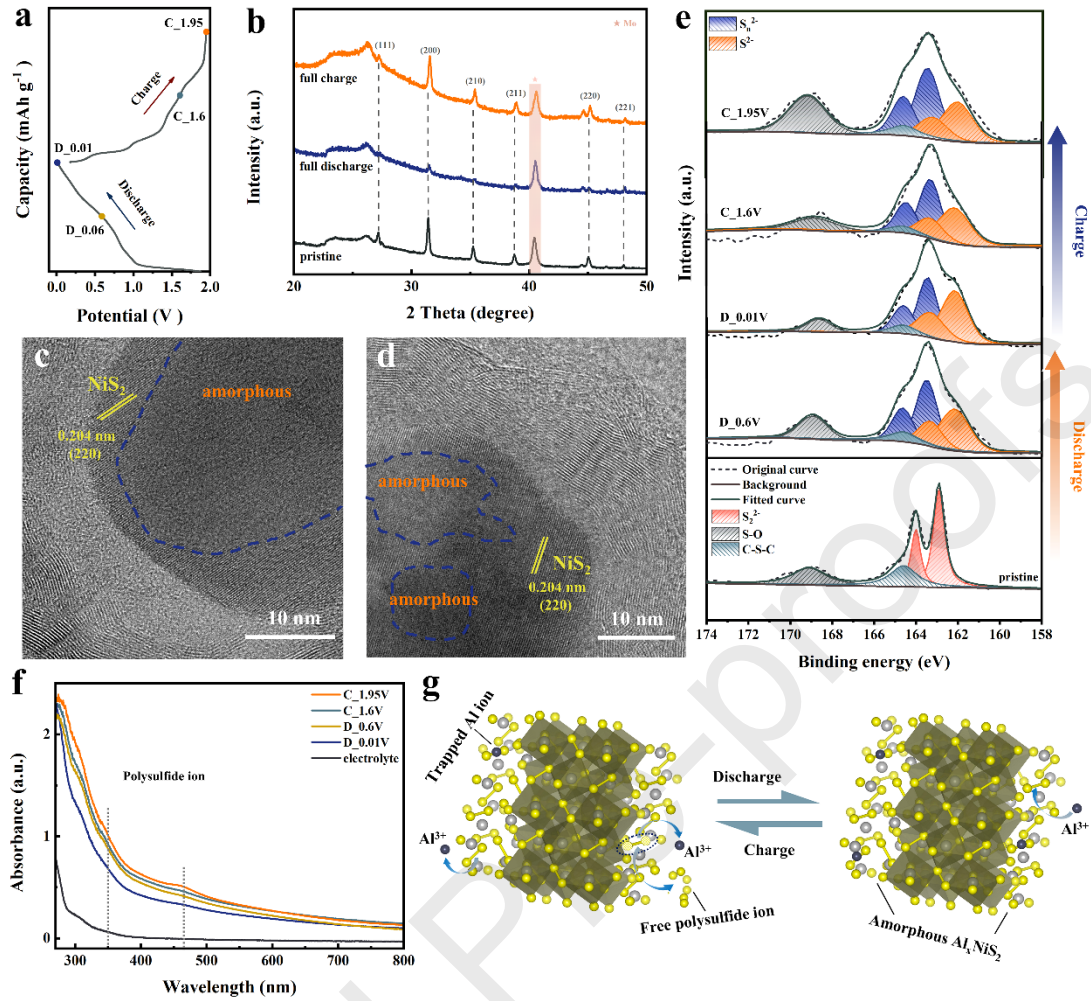


**Figure 4.** (a) Charge/discharge curve at the selected states at  $100 \text{ mA g}^{-1}$  for  $\text{NiS}_2/\text{SC}$  electrode. (b) Ex situ XRD patterns of  $\text{NiS}_2/\text{SC}$  electrode at full-charge and full-discharge state. HRTEM images of  $\text{NiS}_2/\text{SC}$  electrode (c) at full-discharge and (d) full-charge states. (e) S 2p X-ray photoelectron spectra of  $\text{NiS}_2/\text{SC}$  at different states of discharge and charge fitted using two species ( $\text{S}_n^{2-}$  and  $\text{S}^{2-}$ ) in blue and orange. (f) Ultraviolet-visible spectra of the electrolyte at various states. (g) Schematic of the proposed energy-storage mechanisms for  $\text{NiS}_2$ -based cathode.

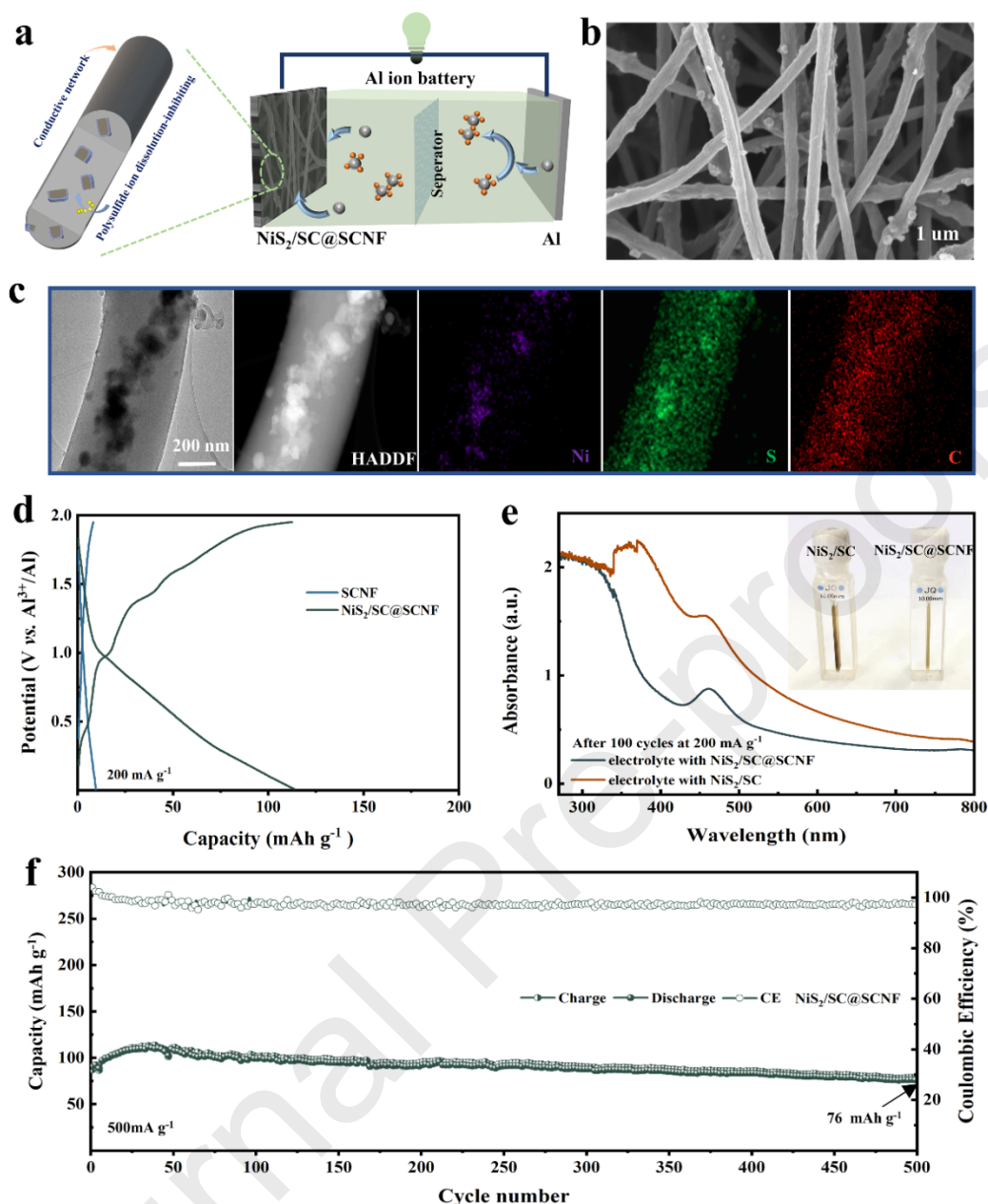
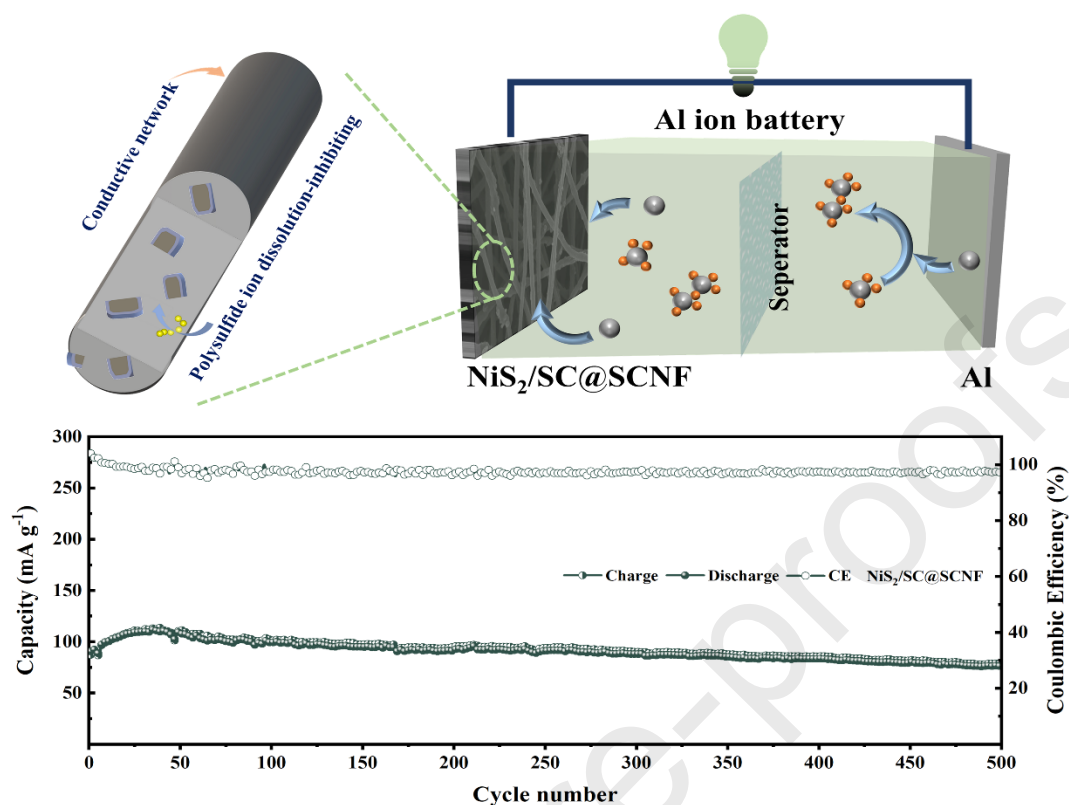


**Figure 5.** (a) Schematic of Al-ion battery during discharge. On the cathode side, Al ion was inserted into NiS<sub>2</sub> structure. On the anode side, Al anode had the typical discharge reaction of  $\text{Al} + 7\text{AlCl}_4^- - 3e^- \rightarrow 4\text{Al}_2\text{Cl}_7^-$ . Morphological and structural features of NiS<sub>2</sub>/SC@SCNF material. (b) SEM and (c) TEM images with the corresponding element mapping (Ni, S, and C). (d) Galvanostatic charge and discharge curves of NiS<sub>2</sub>/SC@SCNF and pure SCNF at 200 mA g<sup>-1</sup>. (e) Ultraviolet-visible spectra and optical photograph (the insert) of the electrolyte with different materials after 200 cycles at 200 mA g<sup>-1</sup>. (f) Long-cycling performance of NiS<sub>2</sub>/SC@SCNF material at 500 mA g<sup>-1</sup>.

## Graphical abstract



As a promising candidate battery for large-scale energy storage, rechargeable aluminum-ion batteries (AIBs) are receiving considerable attention owing to high theoretical capacity and abundance of aluminum. Here, the authors report the electrospun  $\text{NiS}_2$ -based cathode to stabilize anionic redox processes, exhibiting excellent Al storage performance.

## Highlight:

- Preparation of unique  $\text{NiS}_2$  nanomaterials with S-doped carbon coating structure.
- Acquiring the mechanism of  $\text{NiS}_2$ -based cathode material through detailed characterization.
- The  $\text{NiS}_2/\text{SC@SCNF}$  cathode alleviates polysulfide dissolution for durable Al storage.
- Superior cycling stability of  $\text{NiS}_2/\text{SC@SCNF}$  (76 mAh  $\text{g}^{-1}$  after 500 cycles, 97%  $C_{\text{eff}}$ ).